FINAL REPORT

Date of Report:	December 2, 2009
Contract Number:	DTPH56-08-T-000006
Prepared For:	The U.S. Department of Transportation Pipeline and Hazardous Materials Safety Administration
Project Title:	The Effect of Cathodic Protection on Cracking of High-Strength Pipeline Steels, #350
Prepared By:	CANMET Materials Technology Laboratory
Contact Information:	Winston Revie, wrevie@nrcan.gc.ca, 613-992-1703
Authors of Report	R. W. Revie, M. Elboujdaini, and M. Attard

EXECUTIVE SUMMARY

The objective of this study was to establish the effect of cathodic protection (CP) to produce hydrogen that can cause cracking and in-service failures of high-strength pipeline steels, from X-70 to X-120, and to establish the effectiveness of cathodic protection in mitigating cracking (SCC).

A comparison was made among four grades, or strength levels, of pipeline steels, X-70, X80, X-100, and X-120, with respect to ductility in air and in an aqueous solution that was used to simulate ground water. Ductility in solution was measured under four different levels of cathodic protection, ranging from no cathodic protection to 500 mV of overprotection with respect to the usually accepted criterion of −850 mV vs. $Cu/CuSO_4$ reference electrode.

Experiments were carried out by straining during cathodic polarization in a simulated dilute ground water solution (NS-4 solution) saturated with 5% CO_2/95% N_2 (pH approximately 6.8). Strain rates used were 10^{-4} s^{-1} until the stress of 50% of yield was reached, and then the strain rate was reduced to 2×10^{-6} s^{-1}. After failure, the fracture surfaces were characterized by examination using scanning electron microscopy (SEM).

Under cathodic protection, all four steels showed loss of ductility and features of brittle fracture. The loss of ductility under cathodic polarization was larger the greater the strength of the steel and the more active (i.e., more negative) the applied potential. The Ductility Reduction Index (DRI) was defined to quantify the reduction in ductility.

Reduction of ductility during cathodic polarization was attributed to damage caused by hydrogen atoms that are produced by the reduction at the steel surface of hydrogen ions

in solution, i.e., $H^+ + e^- \rightarrow H$. This reaction takes place at the surface of the steel and leads to hydrogen atoms being absorbed into the steel causing degradation of the steel properties.

INTRODUCTION

With the requirements of increasing cost efficiency of transportation by pipeline, particularly in very long pipelines, high strength pipeline steels, up to X-100, are being used, and X-120 has been developed [1]. It is well known that high-strength steels are more susceptible to hydrogen cracking than are low-strength steels [2]. In addition, at potentials of cathodic protection, hydrogen is produced at the steel surface. Hydrogen atoms are produced by the reduction at the steel surface of hydrogen ions in solution, i.e., $H^+ + e^- \rightarrow H$. By the hydrogen recombination reaction, hydrogen atoms recombine forming hydrogen gas, i.e., $H + H \rightarrow H_2$. Those hydrogen atoms that do not recombine are available to be absorbed into the steel, degrading the steel properties and possibly causing cracking. When the environment contains poisons for the hydrogen recombination reaction, such as compounds of sulphur (including H_2S) and arsenic, hydrogen absorption is increased and cracking is intensified [3].

For these reasons, it is prudent to study the susceptibility of high-strength steels to cracking in simulated ground water in the range of electrochemical potentials that are used in cathodic protection.

The objective of this study was to establish the effect of cathodic protection (CP) to produce hydrogen that can cause cracking and in-service failures of high-strength pipeline steels, from X-70 to X-120, and to establish the effectiveness of cathodic protection in mitigating stress corrosion cracking (SCC). Specifically,

A. To establish the effectiveness of cathodic protection to mitigate SCC without causing hydrogen damage;
B. To assess the effects of underprotection and overprotection of CP;
C. To identify the type of cracking that can occur in high-strength pipeline steels under cathodic protection conditions; i.e., transgranular cracking similar to near-neutral pH stress corrosion cracking, or another type of hydrogen damage;
D. To correlate the microstructure and strength levels with hydrogen damage caused by CP; and
E. To identify any additional factors that contribute to susceptibility to hydrogen damage under CP conditions.

EXPERIMENTAL

Steel

Pipe sections of X-70, X-80, X-100 and X-120 material were obtained. All the pipes obtained were 36 inches in diameter, UOE, and longitudinally welded.

Samples were machined from the pipe – without flattening – in the transverse (hoop) direction and remote from the longitudinal weld. A drawing and a photograph of a

tensile sample used for this analysis are shown in Figure 1. The tensile specimens were cylindrical with a gauge diameter of 6.4 mm and a gauge length of 25 mm. This sample design was used for the tensile tests and for the slow-strain-rate experiments.

The 0.2% offset yield strength, ultimate tensile strength, percent elongation, and percent reduction in area were established for each of the four steels in mechanical tests using an Instron Series IX Automated Materials Testing System. Two tensile samples from each steel type were tested. For each steel grade, Vickers microhardness was measured at 19 locations in a through-thickness section of the pipe cut transverse to the pipe axis.

The chemical compositions of the steels were established using a Baird One-Spark Metals Analyzer.

The steel microstructures were characterized using optical microscopy to study the through-thickness section of pipe cut transverse to the pipe axis.

Electrochemical Polarization

The steels were characterized using electrochemical polarization in accordance with ASTM Standard G5-94 [4]. Polarization measurements were conducted in duplicate using a Solartron SI 1287 potentiostat.

The saturated calomel electrode (SCE) was used as the reference electrode. This reference electrode is widely used in laboratory studies because of its stable potential and ease of use. Potentials with respect to the saturated calomel electrode can be readily converted to potential with respect to other reference electrodes, such as the standard hydrogen electrode (SHE) or the saturated copper–copper sulphate ($Cu/CuSO_4$) reference electrode. The potential of the saturated calomel electrode is 0.242 V vs. SHE, and −0.074 V vs. $Cu/CuSO_4$. The commonly accepted potential for cathodic protection of steel is −0.850 V vs. $Cu/CuSO_4$. This potential and its equivalent with respect to other reference electrodes are listed in Table 1, along with the potentials that correspond to 500 mV of overprotection.

The counter electrode was platinum sheet. Samples of each of the four steel grades were used as the working electrodes. The steel samples were polished with emery paper to 800 grit, rinsed with alcohol, dried, and placed in the cell. The measurements were carried out in a simulated dilute ground water, NS-4 solution, saturated with 5% CO_2/95% N_2. The chemical composition of the NS-4 solution is listed in Table 2. Solution pH was approximately 6.8. This solution was deaerated with the gas mixture for at least one hour before the sample was placed in the cell. The solution was deaerated for at least an additional 15 minutes after the sample was placed in the cell and before polarization began. The gas flow was continued during polarization.

The polarization scans were begun at a potential of 250 mV cathodic to the corrosion potential and were carried out in the noble (positive) direction at a rate of 1 mV per second.

Slow-Strain-Rate Experiments

Slow-strain-rate experiments were carried out at room temperature in air and in NS-4 solution saturated with a gas mixture of 5% CO_2/95% N_2. The apparatus, Instron Model 8511-40, is shown in Figure 2. A total of 40 slow-strain-rate experiments were completed, including duplicates.

Samples for the slow-strain-rate experiments were polished with emery paper to 800 grit. Polishing was carried out in the longitudinal direction of the sample. A metal punch with a 1-inch gauge length was used to mark this length on the samples before the slow-strain-rate test. The sample was rinsed with alcohol and dried. Clear nail polish was used to mask the area of the sample outside the 1-inch gauge length. After mounting the sample in the cell, the solution was deaerated with the gas mixture for at least 2 hours, and the deaeration continued for the duration of the slow-strain-rate experiment.

In solution, the tensile specimens were pulled at the constant strain rate of 10^{-4} s^{-1} until the stress reached 50% of the yield strength, at which time the strain rate was reduced to 2×10^{-6} s^{-1}. The slow-strain-rate experiments were carried out under four different experimental conditions:

- Free corrosion potential or open circuit potential (OCP), approximately −0.7 V vs. SCE;
- Cathodic protection at −0.776 V vs. SCE, a potential that is equivalent to −850 mV vs $Cu/CuSO_4$, the cathodic protection potential that is commonly used in operating pipelines;
- Cathodic protection at 100 mV potential shift from the corrosion potential; and
- Cathodic overprotection by 500 mV; i.e. at a potential of −1.276 V. vs. SCE.

The experiments at controlled potential were conducted using a Solartron SI 1287 potentiostat for controlling potential of samples from each steel type (X-70, X-80, X-100 and X-120), Figures 2b and c. Samples that were cathodically polarized during the slow-strain-rate experiment were cathodically pre-charged for 4 hours before the straining began, and this pre-charging began after the 2 hours of deaeration.

Strain was measured in two ways:

1. In the slow-strain-rate experiments in NS-4 solution, strain was determined by measuring, with a micrometer at the end of the test, the increase in length of the one-inch gauge length that had been marked on the sample by using a metal punch before the straining began; and

2. For samples strained in air, strain was also measured using an extensometer, Epsilon Technology Corp. Model 3542-0100-050-LT.

Ductility was assessed by calculating the percentage reduction in area, *RA*, using Equation (1),

$$RA(\%) = \frac{(D_i^2 - D_f^2)}{D_i^2} \times 100 \quad (1)$$

and by calculating the % elongation, *El*, using Equation (2):

$$El(\%) = \frac{l_f - l_i}{l_i} \times 100 \quad (2)$$

where D_i and D_f are the initial and final diameters, respectively, of the tensile specimen, and l_i and l_f are the initial and final gauge lengths, respectively, of the specimen.

At the end of each experiment, the *RA* and the *El* were calculated. After failure, the scanning electron microscope (SEM) was used for fractographic analysis. The results of the experiments in air at room temperature were taken as the reference for ductility as well as for changes in fracture morphology.

RESULTS AND DISCUSSION

Steel

The wall thickness of each of the steels is listed in Table 3, as well as the average results obtained from two tensile samples of each steel. In general, ductility decreases with increasing strength. The results of the microhardness measurements, listed in Table 4, indicate increasing hardness with increasing strength. The chemical compositions of the steels are listed in Table 5.

Photomicrographs of the four steels are shown in Figure 3. The X-70 steel consists mainly of ferrite and a darker etching second phase. The X-80 is comprised of acicular ferrite with bainite, and the X-100 has an ultra-fine bainitic microstructure. In X-120, the microstructure consists of bands of intercritical polygonal ferrite interspersed with a dark etching second phase that is very fine and alternates with larger bands of martensite with some bainite regions.

Electrochemical Characterization

The polarization curves, potential vs. current density, for each of the four steels are shown in Figure 4. The corrosion potentials (i.e., the potentials with no applied current) are reported in Table 6.

Slow-Strain-Rate Experiments

Stress–strain curves for each of the four steels in air as determined in slow-strain-rate experiments are presented in Figure 5.

The data obtained from the slow-strain rate experiments in air and in NS-4 solution are summarised in Table 7. In Figures 6 and 7, the data on percent reduction in area and percent elongation, respectively, are summarized. As reference points for comparison, the data in air for each of the steels are also shown in Figures 6 and 7.

In air, the percent reduction in area and the percent elongation to failure both decrease as the strength of the steel increases.

For each of the steels, the percent reduction in area and percent elongation both decrease in solution, in comparison to the values of these parameters in air. These parameters further decrease as the cathodic polarization increases; i.e., as the potential becomes more active (or more negative) with respect to the reference electrode. In other words, for each steel, the ductility is less in solution than in air, and the ductility decreases further with cathodic protection.

For quantitatively comparing the reduction in ductility that takes place in solution and under cathodic protection conditions, compared with the ductility in air, a ductility reduction index, DRI, is defined as

$$\mathrm{DRI} = \frac{RA_{\mathrm{solution}}}{RA_{\mathrm{air}}} \times 100$$

Values of DRI are listed in Table 8. Ratios in the range of 0.8 to1.0 normally denote high resistance to stress corrosion cracking, whereas low values (i.e., <0.5) show high susceptibility to brittle fracture and cracking [5].

Fracture Characteristics

From the optical macrographs of the profiles of the crack surfaces in X-70 steel in Figures 8a to 8d, the decreased ductility of the specimen polarized at −1.276 V vs. SCE compared with the other specimens is evident. This observation supports the data in Table 7, indicating RA of 69% for X-70 in air, but 22% for X-70 polarized at the level of 500 mV of overprotection. The optical macrograph of the fracture surface in Figure 8e shows the cup-and-cone fracture appearance, typical of ductile fracture, of the X-70 that fractured in air, whereas Figures 8f to 8h show less ductility in solution at the corrosion potential and under cathodic polarization.

SEM macrographs and micrographs of fracture surfaces of X-70 and X-80 steels fractured in air and in solution at the corrosion potential are shown in Figure 9. As the figures show, there is considerably less ductility in the samples fractured in solution than those fractured in air. In air, the specimens showed ductile fracture, Figures 9(a) and 9(e) in X-70 and X-80, respectively. In solution, the specimens showed a brittle fracture (Figures 9(b) and (f)) with a transgranular appearance type of cracking, Figure 9(d).

Figure 10 shows optical macrographs of the profiles of the fracture surfaces of X-70 samples in air and in solution at three different potentials, the corrosion potential, the

cathodic protection potential of −0.776 V vs. SCE, and the overprotection potential of −1.276 V vs. SCE. For each of these four profiles, an SEM micrograph is also presented. Corresponding to the data in Table 7 and Figure 6 for X-70 steel, there is a reduction in ductility of samples fractured in solution compared to those fractured in air, and the sample that was cathodically overprotected at the potential of −1.276 V vs. SCE was the least ductile, or most brittle, of the X-70 samples. The SEM macro-images and photomicrographs of the fracture surfaces in Figure 11 support the results regarding decreased ductility of X-70 steel in solution.

S.E.M. micro-images and photomicrographs are presented in Figure 12 for X-80 steel under the same conditions as for X-70 steel in Figure 11. In Figures 13 and 14, S.E.M. micro-images and photomicrographs are presented for X-100 and X-120 steel, respectively, showing the fracture surfaces after fracture in air, at the corrosion potential, and at two levels of cathodic protection. Optical macrographs are presented in Figure 15 showing the fracture surfaces of X-120 after fracture in air, in solution at the corrosion potential, and in solution at three different levels of cathodic protection.

The images in Figures 8 through 15 all reinforce the observations that ductility of the steels in air decreases with increasing strength of steel, decreases on exposure to aqueous solution, and decreases further with cathodic protection. When any of these steels is stressed to failure in solution, the ductility decreases, and application of cathodic potentials decreases the ductility further. With more active (or more negative) potentials, the ductility is further reduced.

The data in Table 7 and in Figures 6 and 7 indicate that the X-120 steel has the lowest ductility in air of all the steels studied. For this steel, as reported in Table 8, the ductility reduction index, DRI, was calculated to be in the range 0.20 – 0.30, indicating a high susceptibility to cracking in aqueous solution. On the other hand, the DRI for the X-70 and X-80 steels, except at 500 mV of cathodic overprotection, was in the range 0.65 – 0.79, indicating that these steels have more resistance to cracking than does the X-120. At 500 mV of cathodic overprotection, at −1.276 V vs. SCE, the DRI for all the steels was found to be in the range 0.20 – 0.33, indicating a high susceptibility to cracking.

Hydrogen Produced by Cathodic Polarization

In Table 9, the thermodynamic potentials of the hydrogen electrode are indicated at pH values between 6 and 10. These potentials are reported with respect to the Standard Hydrogen Electrode (SHE), the Saturated Calomel Electrode (SCE), and the saturated copper–copper sulphate ($Cu/CuSO_4$) reference electrode. At potentials more negative than those listed in Table 9, hydrogen is produced by the reaction, $H^+ + e^- \rightarrow H$, and this hydrogen can contribute to cracking. These H atoms may recombine form H_2 gas, or, depending on the environment, they may be absorbed into the steel, causing hydrogen damage that can contribute to cracking.

At potentials active to (or more negative than) the reversible potential for the hydrogen equilibrium, hydrogen is produced by the reaction, $H^+ + e \rightarrow H$. The reversible potential for hydrogen, in volts vs. the standard hydrogen electrode (SHE), is given by,

$$\phi_{\text{reversible}} = -0.0592 \times \text{pH}$$

At pH = 7,

$$\phi_{\text{reversible}} = -0.0592 \times 7 = -0.414 \text{ V. vs. SHE}$$

Overpotential is defined by,

$$\eta = \phi_{\text{measured}} - \phi_{\text{reversible}}$$

Assuming that the magnitude of overpotential for hydrogen on steel follows the equation,

$$\eta = 0.105 \log_{10} \frac{i}{1 \times 10^{-7}} = 0.105 \log_{10} (i \times 10^{7}) ,$$

the rate of hydrogen production can be calculated as a function of potential and pH.

At the corrosion potential, −0.750 V. vs. SCE, which corresponds to −0.508 V. vs. SHE, the overpotential is

$$\eta = -0.508 - (-0.414) = -0.094 \text{ V}$$

The rate of hydrogen production, in mL of hydrogen (at S.T.P.) per cm^2 of steel surface per day, is calculated as follows:

$$\eta = 0.105 \log_{10} \frac{i}{1 \times 10^{-7}} = 0.105 \log_{10} (i \times 10^{7}) = 0.094$$

$$\log_{10} (i \times 10^{7}) = \frac{\eta}{0.105} = \frac{0.094}{0.105} = 0.895$$

$i \times 10^{7} = 7.85$

$i = 7.85 \times 10^{-7}$ A/cm^2

$$i = \frac{7.85 \times 10^{-7} C}{\text{cm}^2 \text{ - s}} \times \frac{8.64 \times 10^{4} \text{ s}}{\text{day}} \times \frac{\text{eq}}{96{,}500 \text{ C}} \times \frac{\text{mole H}_2}{2 \text{ eq}} \times \frac{22{,}400 \text{ mL H}_2}{\text{mole H}_2} = 0.0079 \text{ mL/cm}^2 \text{ - day}$$

In the same way, the rates of hydrogen production can be calculated at other potentials. The data presented in Table 10 indicate the increase of hydrogen production with increasingly negative, or increasingly active, potentials.

SUMMARY

The susceptibility to SCC under cathodic protection of the X-70, X-80, X-100 and X-120 pipeline steels was evaluated. Specimens tested in the NS-4 solution saturated with 5%CO_2/N2 presented high susceptibility to SCC, especially in X-100 and X-120 steels.

In the slow-strain-rate experiments, the specimens tested in air exhibited ductile fracture whereas in the NS-4 solution the specimens showed significantly less ductility. Cathodic overprotection resulted in further ductility reduction, an effect that was quantified by the Ductility Reduction Index (DRI).

Hydrogen reduction was considered to be a significant factor in the ductility reduction and fracture processes. Cracking susceptibility was indicated by degradation in mechanical properties (e.g., percent reduction in area and percent elongation) and also the presence of secondary cracking along the gauge length of specimens. Cracking was attributed to the diffusion of atomic hydrogen promoting the embrittlement damage. Crack paths were very irregular with brittle appearance.

IMPACT OF THE RESEARCH RESULTS

The main impact of this study arises because of the effects of cathodic protection on high-strength steels and the need to avoid overprotection to ensure adequate ductility. In drafting revisions to standards on cathodic protection, it would be prudent to insert clause material commenting on precautions that may be necessary to ensure that cathodic protection of high-strength steels is adequately controlled, without overprotection or underprotection.

RECOMMENDATIONS FOR FUTURE RESEARCH

1. To support the conclusions of this study that the decrease in ductility with cathodic protection is caused by hydrogen, it would be most useful to carry out experiments in which the diffusible and total hydrogen content of steel samples after fracture is measured. With information from such experiments, it may be possible to make a quantitative correlation between hydrogen absorption and ductility reduction.

2. In other studies at the CANMET Materials Technology Laboratory, it has been found that some steels are very susceptible to hydrogen-induced cracking (HIC). Susceptibility was related to a threshold hydrogen concentration for HIC and also a threshold pH in the environment for HIC [6–8]. By studying the role of hydrogen in ductility reduction, it is possible that optimization of steel composition and processing would be possible to minimize ductility reduction as a result of exposure to an aqueous environment and cathodic protection.

3. By studying other environments, in addition to the NS-4 solution that was used in this study, it may be possible to identify environments that are particularly

detrimental for hydrogen absorption into the steel and the accompanying ductility reduction. Environments that would be expected to be especially damaging are solutions containing sulphur or arsenic compounds, which can act as poisons for the hydrogen recombination reaction.

ACKNOWLEDGEMENTS

The authors acknowledge the experimental assistance of Bob Eagleson and helpful discussions with Jim Gianetto, Jian Li, and Bill Tyson. Renata Zavadil provided valuable metallographic support. Laurie Collins of Evraz Inc. NA provided helpful support for the project. The assistance of CANMET Engineering Technical Services in machining the tensile samples is gratefully acknowledged.

REFERENCES

1. Haroyuki Makino, Izumi Takeuchi, and Ryouta Higuchi, "Fracture propagation and arrest in high-pressure gas transmission pipeline by ultra high strength line pipes," Proceedings, International Pipeline Conference, Calgary, September 2008, Paper Number IPC2008-64078

2. R. W. Revie and H. H. Uhlig, *Corrosion and Corrosion Control*, 4th edition, Wiley, New York, 2008. pp. 65–66.

3. R. W. Revie and H. H. Uhlig, *Corrosion and Corrosion Control*, 4th edition, Wiley, New York, 2008. pp. 166–167.

4. N. D. Greene, *Experimental Electrode Kinetics*, Rensselaer Polytechnic Institute, Troy, New York, 1965; ASTM Standard G5-94 (Reapproved 1999), *Standard Reference Test Method for Making Potentiostatic and Potentiodynamic Polarization Measurements*, ASTM, West Conshohocken, PA.

5. A. Contreras, A. Albiter, M. Salazar, and R. Perez, "Slow strain rate corrosion and fracture characteristics of X-52 and X-70 pipeline steels," *Materials Science and Engineering* **A407**, 45-52 (2005).

6. R. W. Revie, V. S. Sastri, G. R. Hoey, R. R. Ramsingh, D. K. Mak, and M. T. Shehata, "Hydrogen-Induced Cracking of Linepipe Steels; Part 1 – Threshold Hydrogen Concentration and pH," *Corrosion*, **49** (1), 17 (1993).

7. M. Elboujdaini, V. S. Sastri, and R. W. Revie, "Field Measurement of Hydrogen in Sour Gas Pipelines," *Corrosion*, **50** (8), 636 (1994).

8. D. R. Morris, V. S. Sastri, M. Elboujdaini, and R. W. Revie, "Electrochemical Sensors for Monitoring Hydrogen in Steel," *Corrosion*, **50** (8), 641 (1994).

Table 1. Potentials for cathodic protection and for 500 mV of overprotection of steel, with respect to three different reference electrodes

	Potential		
	V vs. $Cu/CuSO_4$	V vs. SCE	V vs. SHE
Cathodic protection	−0.850	−0.776	−0.534
500 mV of overprotection	−1.350	−1.276	−1.034

Table 2. Composition of near-neutral pH electrolyte, NS-4 solution

Compound	$NaHCO_3$	KCl	$CaCl_2$	$MgSO_4 \cdot 7H_20$
Concentration (g/L)	0.483	0.122	0.137	0.131

Table 3. Wall Thickness and Tensile Test Data

Steel Grade	**Wall Thickness**	**Yield Strength**		**Ultimate Tensile Strength**		**Elongation (%)**	**Reduction in Area (%)**
	Inch	**MPa**	**ksi**	**MPa**	**ksi**		
X-70	0.529	530.3	76.9	603.7	87.6	28.5	66.7
X-80	0.50	632.1	91.7	717.8	104.1	27.6	62.7
X-100	0.750	807.2	117.1	872.2	126.5	19.1	52.0
X-120	0.625	846.0	122.7	941.8	136.6	16.1	53.0

Table 4. Microhardness Data

Steel Grade	**Vickers Microhardness (300 g)**		
	Average	**Standard Deviation**	**Range**
X-70	206	6	Max. 217
			Min. 192
X-80	236	6	Max. 246
			Min. 227
X-100	272	11	Max. 286
			Min. 238
X-120	302	29	Max. 362
			Min. 267

Table 5. Chemical compositions of steels

Element (%)	Steel Grade			
	X-70	**X-80**	**X-100**	**X-120**
Carbon	0.069	0.039	0.077	0.071
Manganese	1.46	1.62	1.80	1.8
Silicon	0.24	0.13	0.097	0.094
Phosphorus	0.014	0.009	0.007	0.009
Sulfur	< 0.002	< 0.002	< 0.002	<0.002
Chromium	–	0.45	0.030	0.040
Nickel	–	0.13	0.49	0.13
Molybdenum	–	< 0.005	0.28	0.22
Copper	0.006	0.26	0.29	0.25
Aluminium	0.043	0.038	0.035	0.018
Niobium	0.060	0.095	0.031	0.044
Vanadium	0.053	0.0046	0.0038	0.004
Titanium	0.013	0.016	0.009	0.010
Calcium	0.0015	0.0015	< 0.001	0.001

Table 6. Corrosion Potentials

Steel Type	ϕ_{corr}, **V vs. SCE**
X-70	−0.751
X-80	−0.735
X-100	−0.724
X-120	−0.680

Table 7. Results of slow-strain-rate experiments in air and in NS-4 solution.

Steel Grade	Parameter	In Air			In NS-4 Solution											
					Corrosion Potential, ϕ_{corr}, V vs. SCE			CP Potential (−0.776 V vs. SCE)			ϕ_{corr} − 0.100 V			CP Potential − 0.500 V (−1.276 V vs. SCE)		
		Test 1	Test 2	Avg.	Test 1	Test 2	Avg.	Test 1	Test 2	Avg.	Test 1	Test 2	Avg.	Test 1	Test 2	Avg.
X-70	Post Test Diameter (mm)	3.52	3.58	**3.55**	4.53	4.59	**4.56**	4.62	4.55	**4.59**	4.73	4.32	**4.53**	5.72	5.58	**5.65**
	Post Test Length (mm)	32.74	32.58	**32.66**	31.34	30.76	**31.05**	31.05	30.99	**31.02**	30.89	31.00	**30.95**	29.06	29.00	**29.03**
	% RA	69.75	68.71	**69.23**	49.90	48.56	**49.23**	47.89	49.46	**48.68**	45.38	54.44	**49.91**	20.12	23.98	**22.05**
	% Elong.	28.90	28.27	**28.59**	23.39	21.10	**22.25**	22.24	22.01	**22.13**	21.61	22.05	**21.83**	14.41	14.17	**14.29**
X-80	Post Test Diameter (mm)	3.86	3.83	**3.85**	4.57	4.50	**4.54**	4.57	4.86	**4.72**	4.86	4.90	**4.88**	5.7	5.68	**5.69**
	Post Test Length (mm)	31.99	32.17	**32.08**	30.36	31.00	**30.68**	30.68	30.33	**30.51**	29.76	30.15	**29.96**	28.95	28.93	**28.94**
	% RA	63.62	64.19	**63.91**	49.01	50.56	**49.78**	49.01	42.33	**45.67**	42.33	41.38	**41.86**	20.68	21.23	**20.96**
	% Elong.	25.94	26.65	**26.30**	19.53	22.05	**20.79**	20.79	19.41	**20.10**	17.17	18.70	**17.94**	13.98	13.90	**13.94**
X-100	Post Test Diameter (mm)	4.05	3.73	**3.89**	5.37	5.19	**5.28**	5.44	5.39	**5.42**	5.47	5.35	**5.41**	5.86	5.78	**5.82**
	Post Test Length (mm)	29.86	29.75	**29.81**	28.59	29.07	**28.83**	28.65	29.26	**28.96**	28.71	29.03	**28.87**	27.42	27.76	**27.59**
	% RA	59.95	66.03	**62.99**	29.6	34.24	**31.92**	27.75	29.07	**28.41**	26.95	30.12	**28.54**	16.16	18.44	**17.30**
	% Elong.	17.56	17.13	**17.35**	12.56	14.45	**13.50**	12.80	15.20	**14.00**	13.03	14.29	**13.66**	7.95	9.29	**8.62**
X-120	Post Test Diameter (mm)	4.56	4.57	**4.57**	5.96	5.88	**5.92**	5.92	5.91	**5.92**	6.00	6.02	**6.01**	6.01	6.13	**6.07**
	Post Test Length (mm)	28.83	29.08	**28.96**	27.46	27.73	**27.60**	27.56	27.20	**27.38**	27.27	27.47	**27.37**	27.01	27.10	**27.06**
	% RA	49.23	49.01	**49.12**	13.28	15.59	**14.44**	14.44	14.73	**14.59**	12.11	11.52	**11.82**	11.82	8.26	**10.04**
	% Elong.	13.50	14.49	**14.00**	8.11	9.17	**8.64**	8.50	7.09	**7.80**	7.36	8.15	**7.76**	6.34	6.69	**6.52**

Data on % Elongation in this table were obtained by measuring with a micrometer, at the end of the test, the increase in length of the one-inch gauge length marked on each sample before the test using a metal punch.

Table 8. Ductility Reduction Index (DRI) calculated from measurements of reduction of area in slow-strain-rate experiments.

Steel	**Test Environment**	$RA(\%) = \frac{(D_i^2 - D_f^2)}{D_i^2} \times 100$	$\text{DRI} = \frac{RA_{\text{solution}}}{RA_{\text{air}}}$
X-70	Air	69.23	N/A
	ϕ_{corr}	49.23	0.71
	CP Potential (−0.776 V_{SCE})	48.68	0.70
	ϕ_{corr} − 0.100 V	49.91	0.72
	CP Potential −0 .500 V (ϕ = −1.276 V_{SCE})	22.05	0.32
X-80	Air	63.91	N/A
	ϕ_{corr}	49.78	0.79
	CP Potential (−0.776 V_{SCE})	45.67	0.71
	ϕ_{corr} − 0.100 V	41.86	0.65
	CP Potential −0 .500 V (ϕ = −1.276 V_{SCE})	20.96	0.33
X-100	Air	62.99	N/A
	ϕ_{corr}	31.92	0.51
	CP Potential (−0.776 V_{SCE})	28.41	0.45
	ϕ_{corr} − 0.100 V	28.54	0.45
	CP Potential −0 .500 V (ϕ = −1.276 V_{SCE})	17.30	0.27
X-120	Air	49.12	N/A
	ϕ_{corr}	14.44	0.30
	CP Potential (−0.776 V_{SCE})	14.59	0.30
	ϕ_{corr} − 0.100 V_{SCE}	11.82	0.24
	CP Potential −0 .500 V (ϕ = −1.276 V_{SCE})	10.04	0.20

Table 9. Thermodynamic potentials of the hydrogen electrode calculated for pH values between 6 and 10

pH	**Hydrogen electrode potential**		
	V vs. SHE	**V vs. SCE**	**V vs. $Cu/CuSO_4$**
6	–0.355	–0.597	–0.671
7	–0.414	–0.656	–0.730
8	–0.474	–0.716	–0.790
9	–0.533	–0.775	–0.819
10	–0.592	–0.834	–0.908

Table 10. Effect of Potential on Rate of Hydrogen Production at a Cathode at pH 7

pH	Reversible Potential of the Hydrogen Electrode, $\phi_{reversible}$	Potential, ϕ		Overpotential, $\eta = \phi - \phi_{reversible}$	Rate of hydrogen production
	V vs. SHE	V vs. SCE	V vs. SHE	V	mL H_2/cm^2-day at S.T.P.
7	−0.414	−0.750	−0.508	−0.094	0.0079
		−0.776	−0.534	−0.120	0.014
		−0.850	−0.608	−0.194	0.071
		−1.276	−1.034	−0.620	796

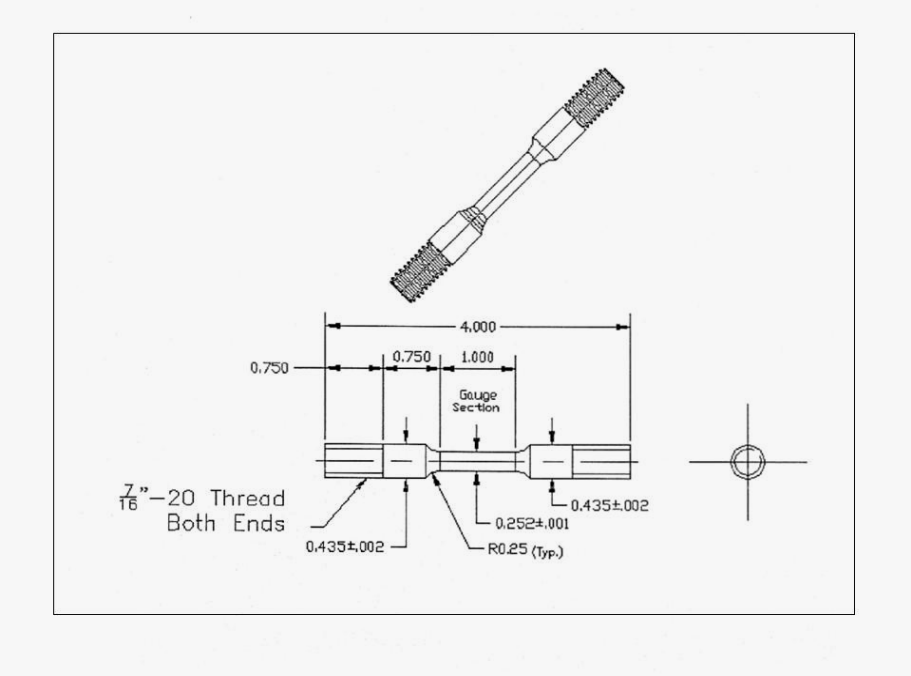

Figure 1. Engineering drawing and photograph indicating the dimensions of the tensile samples used in this project.

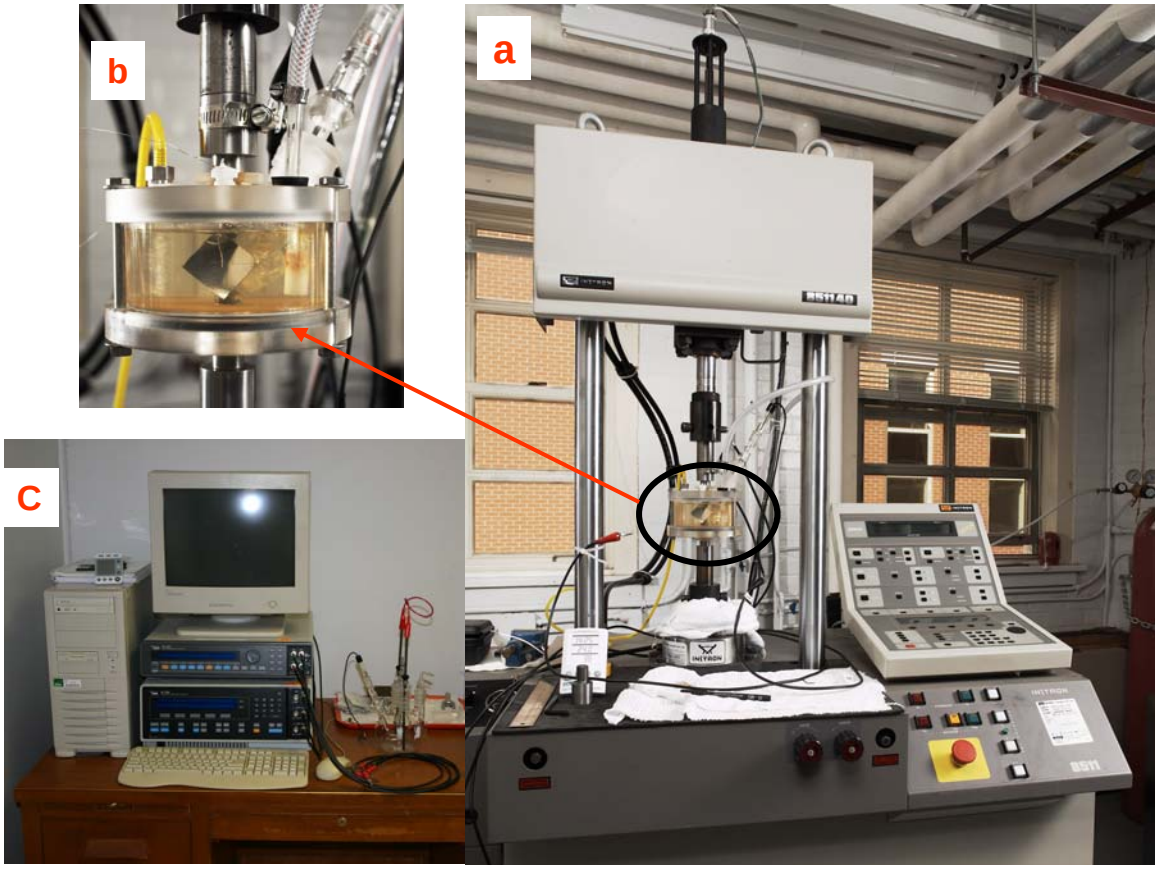

Figure 2. Instron 8511-40 tensile testing machine, showing the electrochemical cell with the gas inlet, saturated calomel reference electrode (SCE); the electrical connections for the working, counter, and reference electrodes; and the Instron control panel that is used for controlling strain rate and other mechanical parameters.

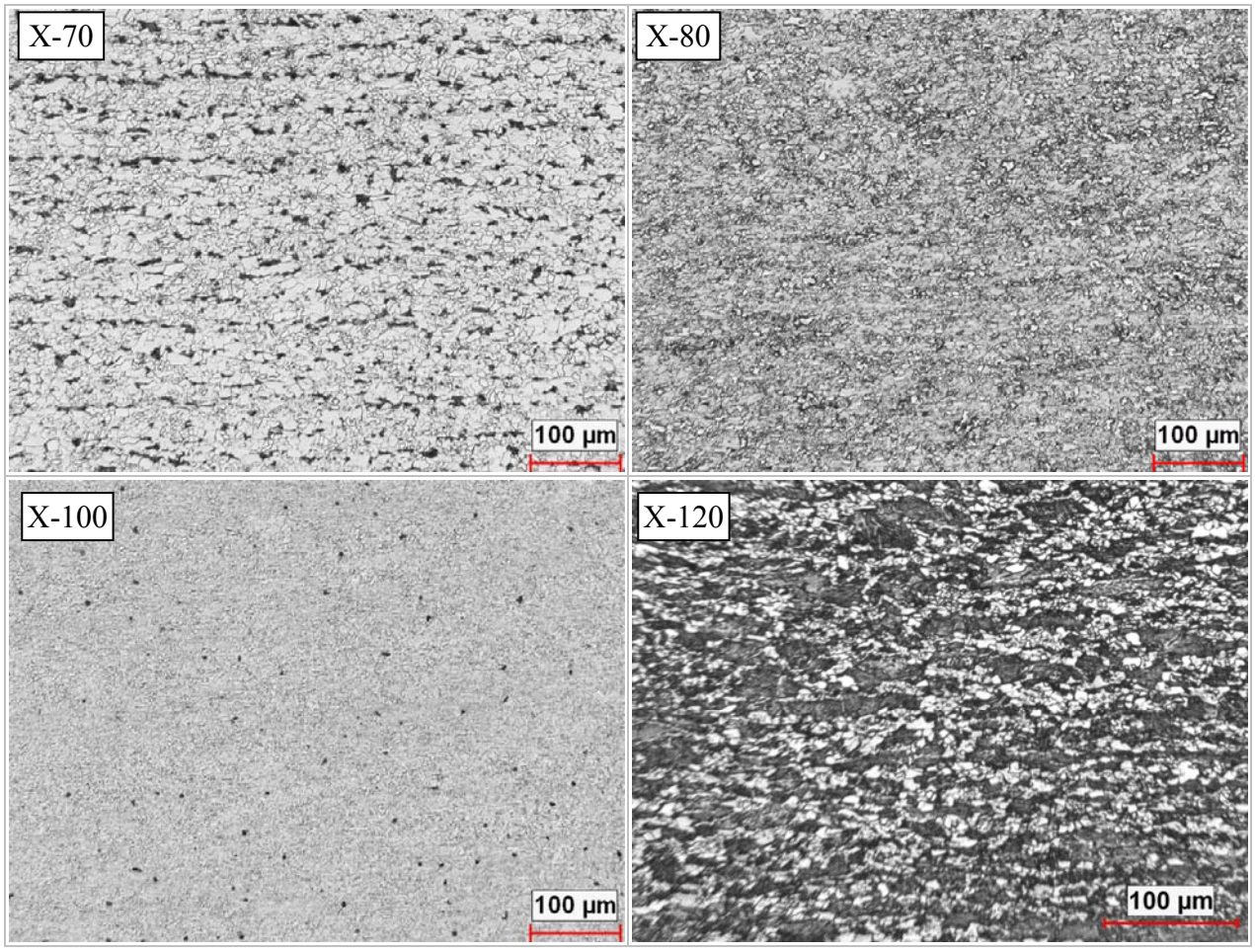

Figure 3. Optical micrographs of steels X-70, X-80, X-100, and X-120, etched with 2% Nital. These images show the microstructure in a through-thickness section of the pipe cut transverse to the pipe axis.

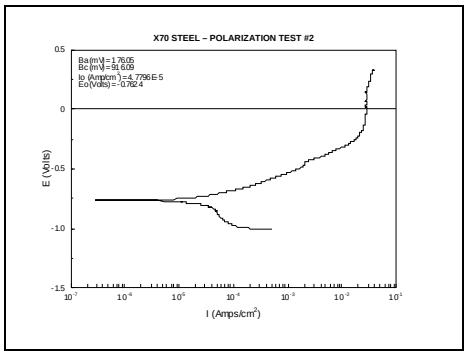

X-70

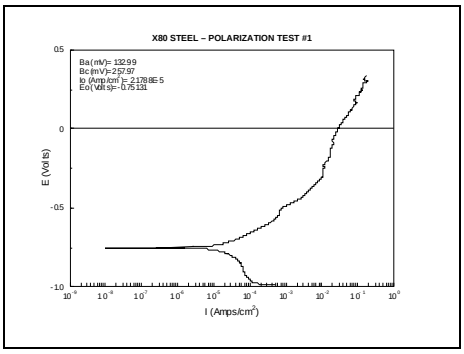

X-80

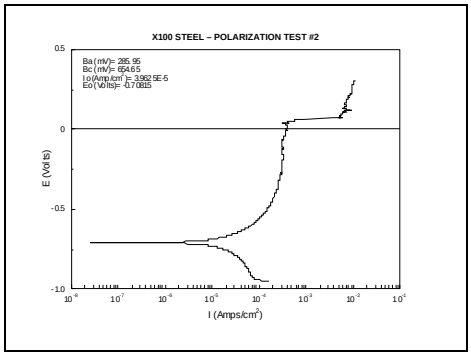

X-100

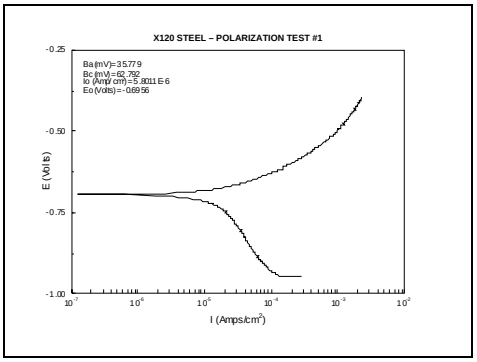

X-120

Figure 4. Potentiodynamic curves of X-70, X-80, X-100, and X-120 pipeline steels in the NS-4 solution saturated with 5% CO_2 / balance N_2 gas mixture, at room temperature and pH 6.8.

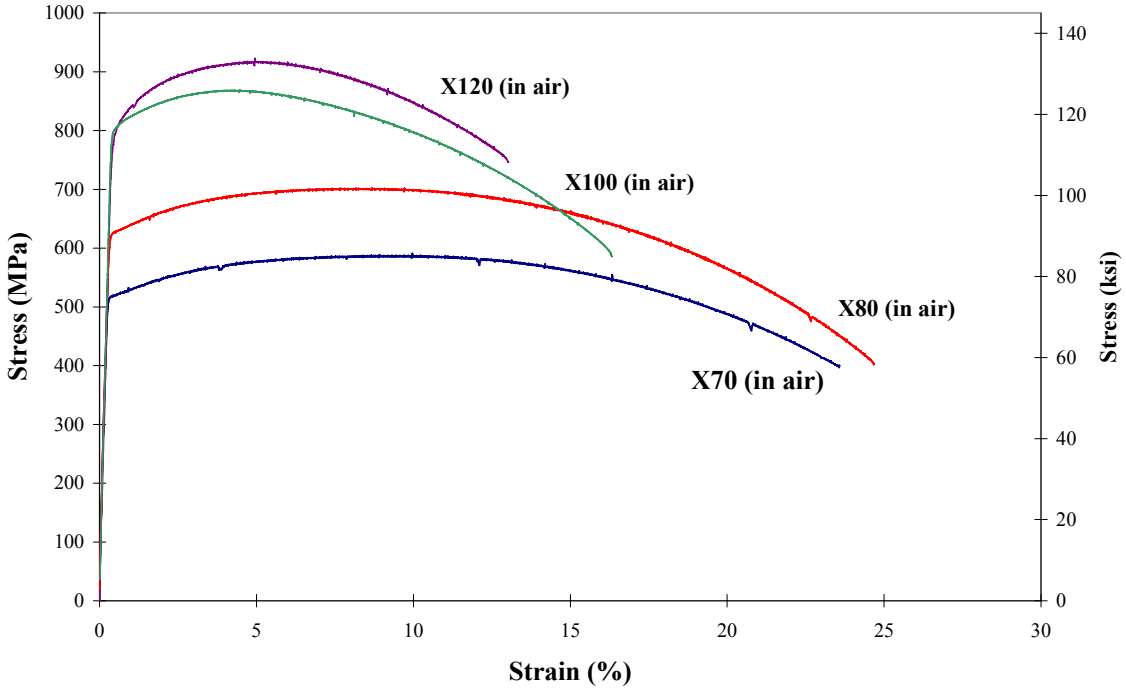

Figure 5. Stress–strain curves for four steels, X-70 to X-120, determined in slow-strain-rate experiments in air. Strain measured using extensometer.

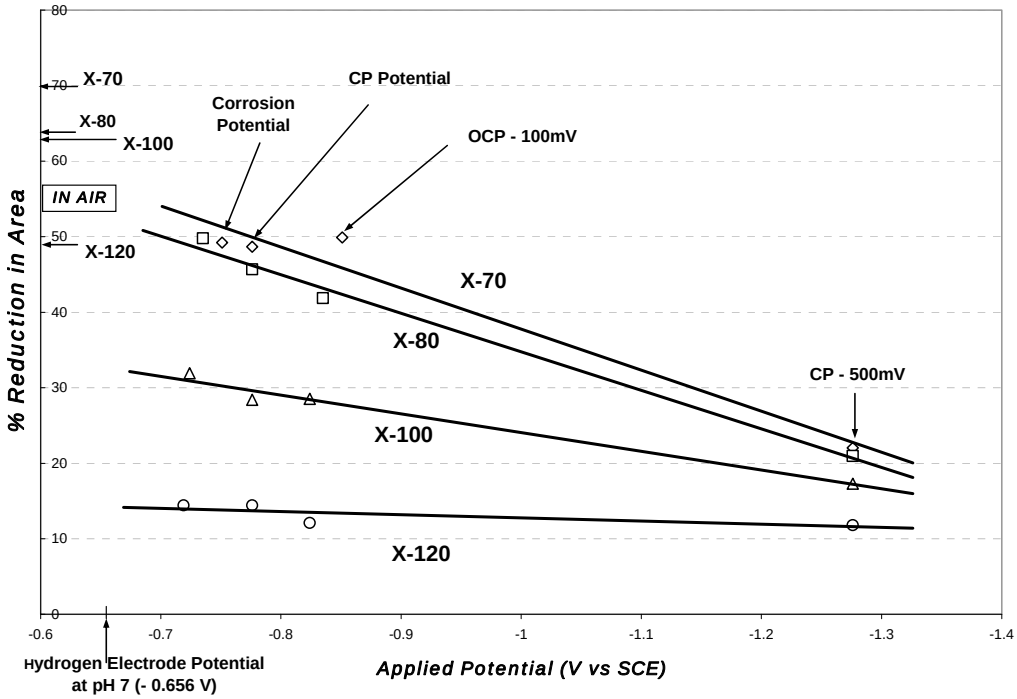

Figure 6. Effect of potential on percent reduction in area in NS-4 solution of the four steels studied. For each steel, the percent reduction in area in air is shown as a reference.

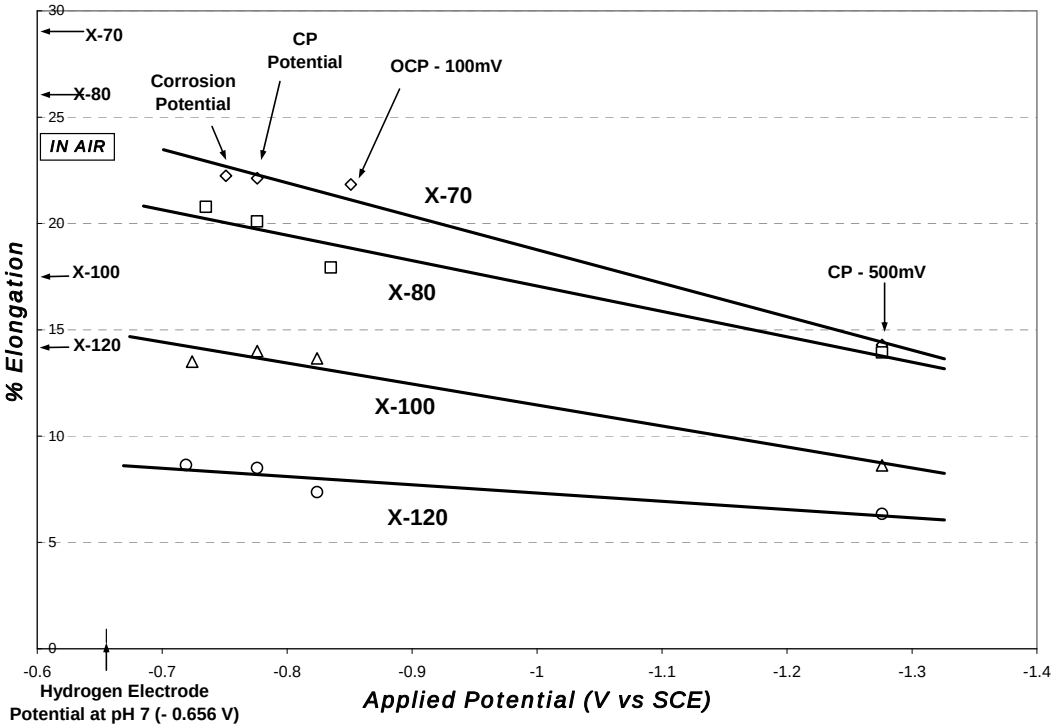

Figure 7. Effect of potential on percent elongation in NS-4 solution of the four steels studied. For each steel, the percent elongation in air is shown as a reference.

Macroscopic Views of Fracture Surface Profiles

X-70 in air

a

X-70 at the corrosion potential (~ −0.7 V)

B

X-70 with CP (−0.776 V vs. SCE)

c

X-70, CP − 0.5 V = −1.276 V vs. SCE)

D

Macroscopic Views of Fracture Surfaces

X-70 in **air**

e

X-70 at the corrosion potential (~ −0.7 V)

f

X-70 – CP (−0.776 V vs. SCE)

g

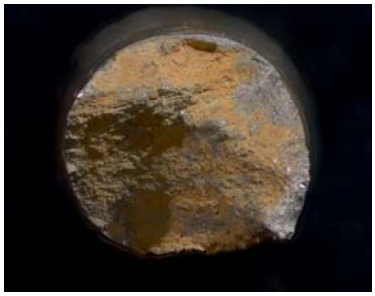

X-70 (CP- 0.5 V = −1.276V vs. SCE)

h

Figure 8. Optical macrographs of fractures of X-70 tensile specimens after slow-strain-rate experiments in air and in solution at three different potentials.

X-70 steel

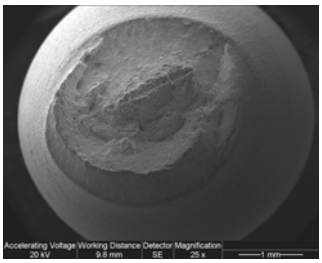

(a) X-70 (in air) x25

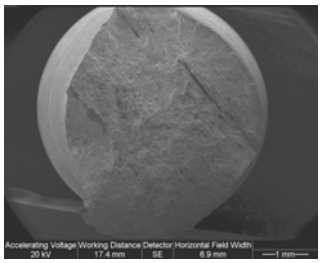

(b) X-70, at the corrosion potential, x18

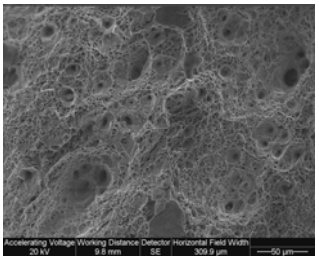

(c) X-70 (in air) x400

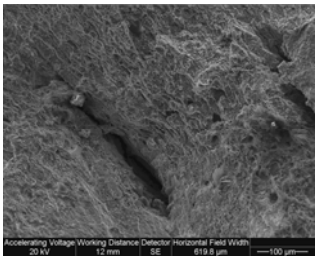

(d) X-70, at the corrosion potential, x200

X-80 steel

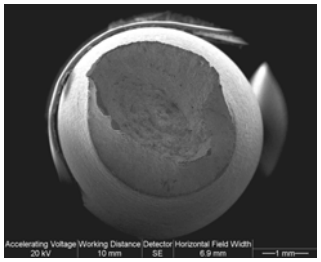

(e) X-80 (in air) x18

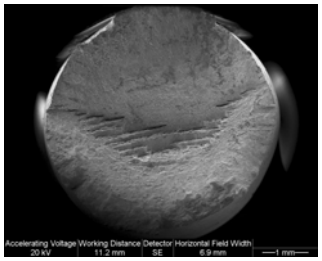

(f) X-80 at the corrosion potential, x18

Figure 9. SEM macrographs and micrographs of fracture surfaces for X-70 and X-80 steels.
(a), (c), and (e) fracture surfaces of samples tested in air, showing ductile fracture;
(b), (d), and (f) fracture surfaces of samples tested in a NS-4 solution at the corrosion potential, showing less ductile, or more brittle, fracture.

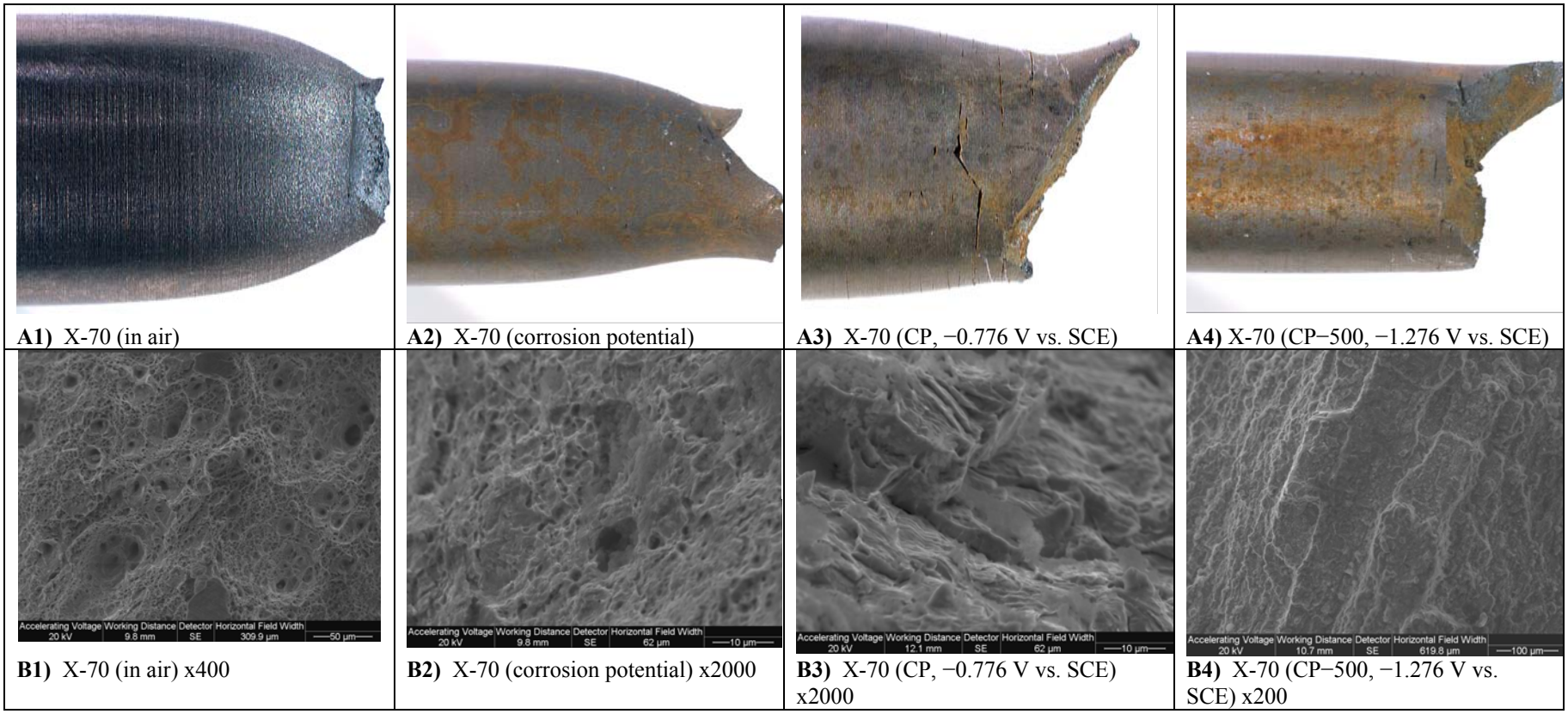

A1) X-70 (in air)

A2) X-70 (corrosion potential)

A3) X-70 (CP, −0.776 V vs. SCE)

A4) X-70 (CP−500, −1.276 V vs. SCE)

B1) X-70 (in air) x400

B2) X-70 (corrosion potential) x2000

B3) X-70 (CP, −0.776 V vs. SCE) x2000

B4) X-70 (CP−500, −1.276 V vs. SCE) x200

Figure 10. Material X-70 Steel

A1, A2, A3, A4 Macro-images of fracture surface profiles: A1, Air; A2, in solution at the corrosion potential; A3, in solution at the cathodic protection potential, −0.776 V vs. SCE; A4, in solution, 500 mV of cathodic overprotection, −1.276 V vs SCE.

B1, B2, B3, B4 S.E.M. photomicrographs of fracture surfaces, same conditions as in A1 to A4.

X-70 Steel

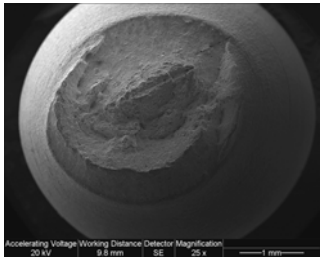
X-70 (in air) img03 x25

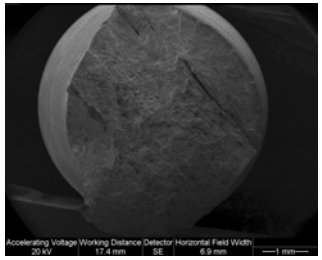
X-70 (corrosion potential) img01 x18

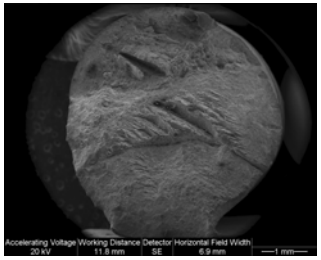
X-70 (CP, −0.776 V vs. SCE) img02 x18

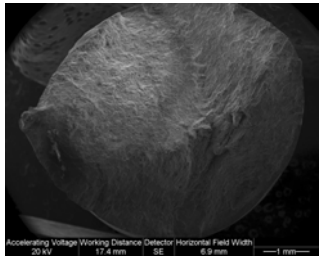
X-70 (CP−500 mV, −1.276 V vs. SCE) img02 x18

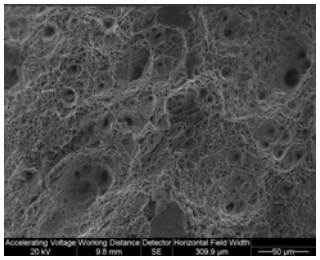
X-70 (in air) img02 x400

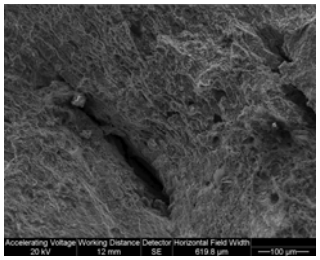
X-70 (corrosion potential) img04 x200

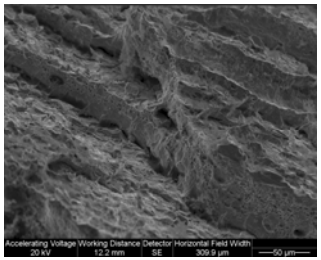
X-70 (CP, −0.776 V vs. SCE) img03 x400

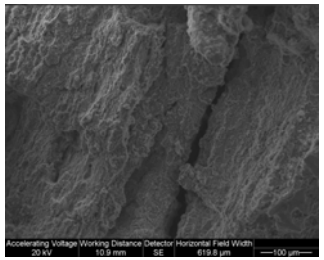
X-70 (CP−500 mV, −1.276 V vs. SCE) img03 x200

Figure 11. S.E.M. macro-images and photomicrographs of X-70 fracture surfaces: in air; in solution, at the corrosion potential, under cathodic protection at −0.776 V vs. SCE, and under 500 mV of cathodic overprotection, at −1.276 V vs. SCE.

X-80 Steel

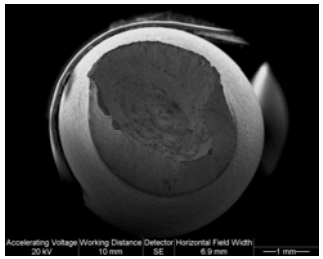
X-80 (in air) img01 x18

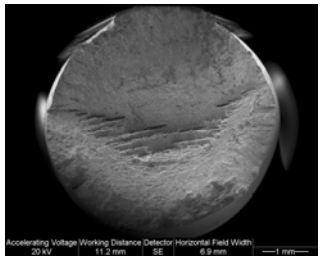
X-80 (corrosion potential) img01 x18

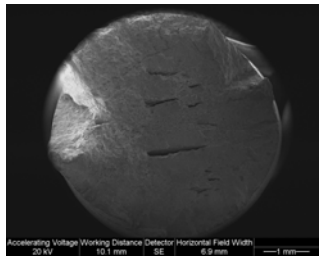
X-80 (CP, −0.776 V vs. SCE) img01 x18

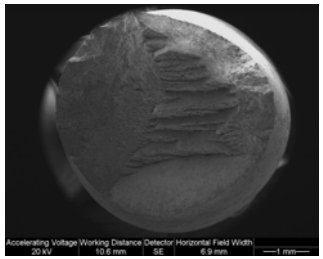
X-80 (CP, −1.276 V vs. SCE) img01 x18

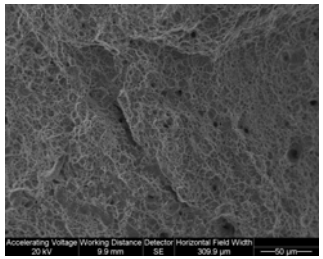
X-80 (in air) img04 x400

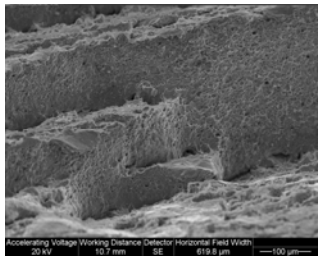
X-80 (corrosion potential) img04 x200

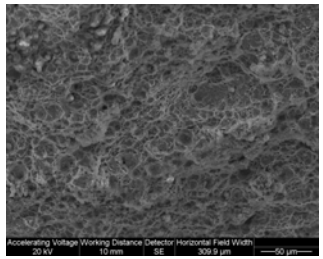
X-80 (CP, −0.776 V vs. SCE) img07 x400

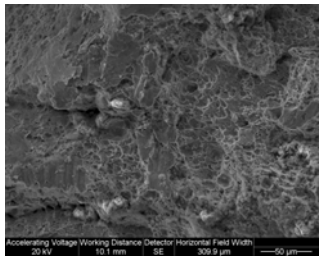
X-80 (CP, −1.276 V vs. SCE) img05 x400

Figure 12. S.E.M. macro-images and photomicrographs of X-80 fracture surfaces: in air; in solution, at the corrosion potential, under cathodic protection at −0.776 V vs. SCE, and under 500 mV of cathodic overprotection, at −1.276 V vs. SCE.

X-100 Steel

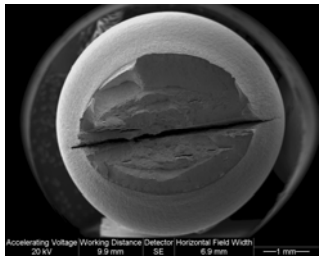

X-100 (in air) img01 x18

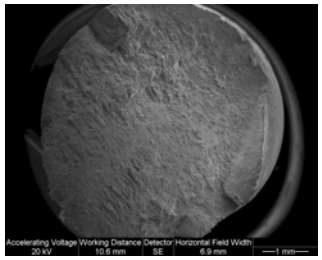

X -100 (corrosion potential) img01 x18

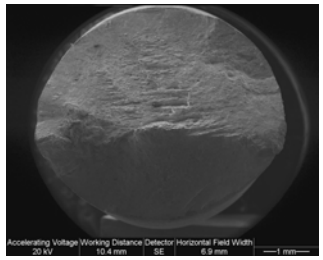

X -100 (ϕ_{corr} − 100 mV) img01 x18

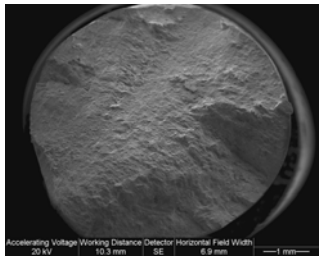

X -100 (CP−500 mV, −1.276 V vs. SCE) img01 x18

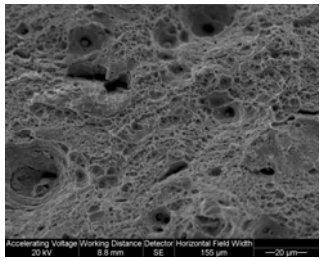

X -100 (in air) img06 x800

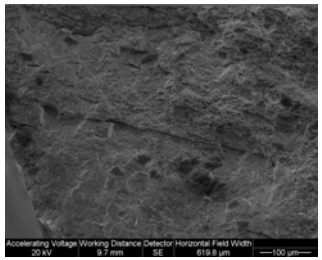

X -100 (corrosion potential) img07 x200

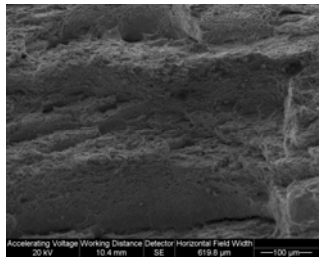

X -100 (ϕ_{corr} − 100 mV) img03 x200

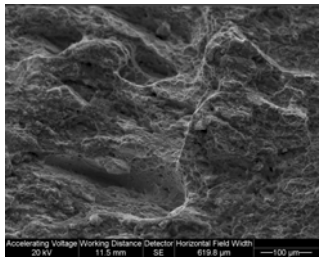

X -100 (CP−500, −1.276 V vs. SCE) img03 x200

Figure 13. S.E.M. macro-images and photomicrographs of X-100 fracture surfaces: in air; in solution, at the corrosion potential, at 100 mV of cathodic protection, and at 500 mV of cathodic overprotection (−1.276 V vs. SCE).

X-120 Steel

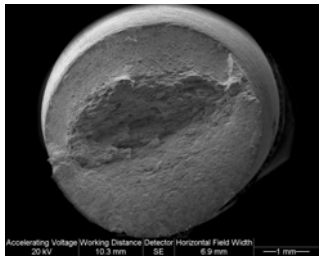
X -120 (in air) img01 x18

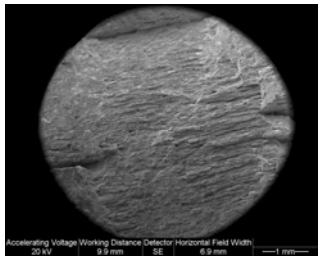
X -120 (corrosion potential) img01 x18

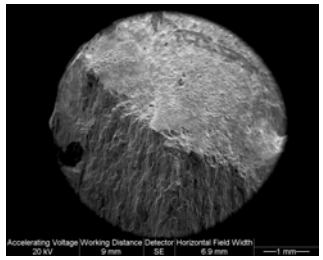
X -120 (ϕ_{corr} − 100 mV) img01 x18

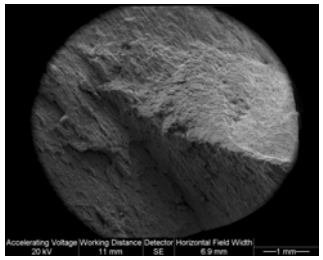
X -120 (CP−500 mV) img01 x18

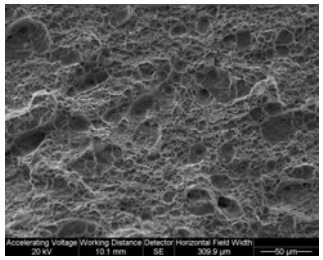
X -120 (in air) img03 x400

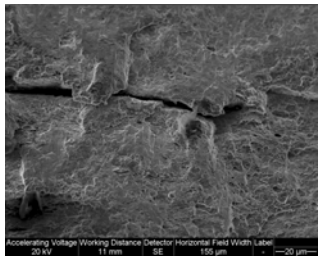
X -120 (corrosion potential) img04 x400

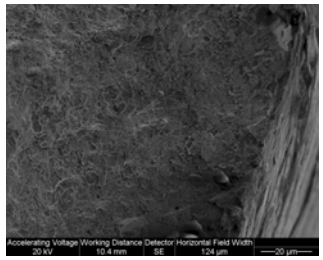
X -120 (ϕ_{corr} − 100 mV) img04 x400

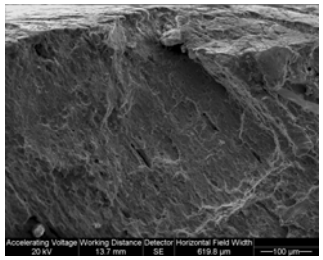
X -120 (CP−500 mV) img06 x200

Figure 14. S.E.M. macro-images and photomicrographs of X-120 fracture surfaces: in air; in solution, at the corrosion potential, with cathodic protection at 100 mV active (negative) to the corrosion potential, and under 500 mV of cathodic overprotection, at −1.276 V vs. SCE.

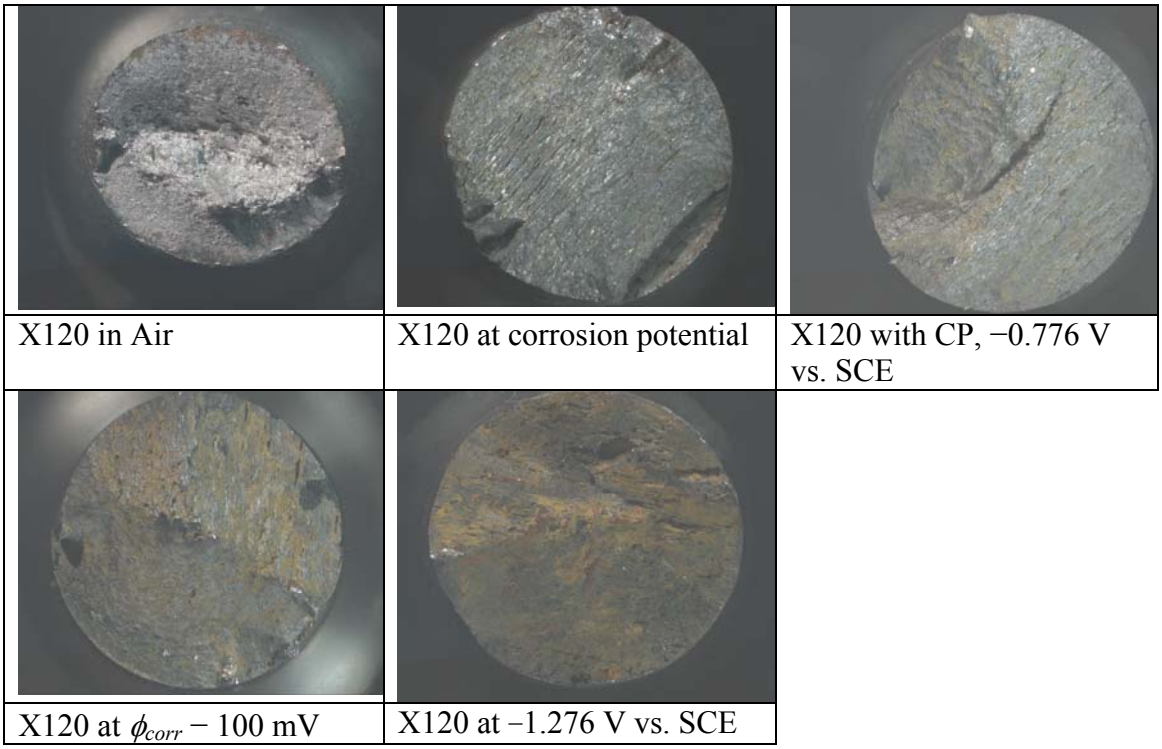

Figure 15. Optical macrographs of X-120 fracture surfaces in slow-strain-rate experiments:
In air;
In solution, at the corrosion potential,
Cathodic protection at −0.776 V vs. SCE,
Cathodic protection at 100 mV active (negative) to the corrosion potential, and
At 500 mV of cathodic overprotection, −1.276 V vs. SCE.

FINANCIAL SECTION

Task Number	Total, $		DOT, $			Cost-share amount, $	
	Planned	Actual	Planned	Previously Billed	To Be Billed	Planned	Actual
1	6,111	6,111	555	555	0	5,556	5,556
2	10,166	18,000	5,083	5,083	0	5,083	12,917
3	10,948	12,000	5,474	4,733	741	5,474	6,526
4	67,148	106,539	33,576	14,369	19,207	33,576	72,963
5	18,450	18,450	9,227	3,075	6,152	9,227	9,223
Total	**112,823**	**161,100**	**53,915**	**27,815**	**26,100**	**58,916**	**107,185**